



# Morphological control of TiO<sub>2</sub> anatase nanoparticles: What is the good surface property to obtain efficient photocatalysts?

Fabien Dufour<sup>a,1</sup>, Stéphanie Pigeot-Remy<sup>a,2</sup>, Olivier Durupthy<sup>a,\*</sup>, Sophie Cassaignon<sup>a</sup>, Valérie Ruaux<sup>b</sup>, Stéphane Torelli<sup>c</sup>, Laurence Mariey<sup>b</sup>, Françoise Maugé<sup>b</sup>, Corinne Chanéac<sup>a</sup>

<sup>a</sup> Sorbonne Universités, UPMC Univ Paris 06, CNRS, Collège de France, Laboratoire de Chimie de la Matière Condensée de Paris, 11 Place Marcelin Berthelot, 75005 Paris, France

<sup>b</sup> Laboratoire de Catalyse et Spectrochimie de Caen, EnsiCaen, Université de Caen, CNRS, 6 Boulevard Maréchal Juin, 14050 Caen, France

<sup>c</sup> CEA, DSV, iRTSV, Laboratoire de Chimie et Biologie des Métaux, F-38054 Grenoble, France

## ARTICLE INFO

### Article history:

Received 28 November 2014

Received in revised form 3 March 2015

Accepted 10 March 2015

Available online 12 March 2015

### Keywords:

TiO<sub>2</sub>  
Morphology  
Photocatalysis  
Surface acidity  
ESR

## ABSTRACT

The richness of titanium dioxide sol-gel syntheses described in literature provided a set of four different morphologies of pure anatase nanoparticles to study the impact of the exposed surfaces on the photocatalytic efficiency of the corresponding material. The selection of the experimental parameters such as the temperature, the heating method or organic additives allowed the synthesis of pure anatase materials with significantly different shapes. A thorough microscopic study of these particles gave the exposed crystallographic faces. The photocatalytic activity of the different materials was estimated following the degradation of the rhodamine B dye under UV-light and significantly different behaviors were observed. In the applied photodegradation conditions, two samples were shown to be more efficient than the reference photocatalyst P25. The rationalization of these results was done through the study of the oxide surface properties, using FT-IR spectroscopy with pyridine as a surface probe and the EPR analysis of photogenerated radicals under UV light. The most efficient photocatalyst for rhodamine B degradation was found to be the morphology presenting the stronger acidic surface sites.

© 2015 Elsevier B.V. All rights reserved.

## 1. Introduction

TiO<sub>2</sub> (titania) is a key industrial material used in a large span of application and more specifically, it is widely studied for its photoelectronic properties [1–4]. The anatase metastable phase is generally proposed as the most efficient polymorph for applications such as dye sensitized solar cells [5] and photocatalysis [6,7]. Thanks to the expression of relatively low energy surfaces,

anatase is actually the most stable TiO<sub>2</sub> structure for small nanometric size [8] and can be prepared using various low temperature syntheses methods [1]. An impressive number of different experimental conditions gave rise to a whole zoology of nanoparticles morphologies from classical truncated square bipyramids, to rods, needles, cubes, squares plates, belts or even hollow rods. Most of them were evaluated in terms of photocatalytic efficiency more or less accurately sometimes using different pollutants and different experimental degradation conditions. Yet in many studies, a clear correlation between the morphology and the photocatalytic efficiency is not given. This is most of the time due to the difficulties obtaining well defined surface and consequently to the absence of its careful description. For instance, in the specific case of anatase nanoplatelets exposing mainly {001} faces it is still not completely clear whether the good activity is due to the presence of the high energy surface itself or to the fluoride leftovers on that surface due to the preparation method [9]. Moreover, the comparison of different anatase morphologies whose photocatalytic efficiencies are described in different articles is very often impossible due to the large differences in the photocatalysis procedure. Overall, the

\* Corresponding author. +33 144271568.

E-mail addresses: [fabien.dufour@fr.michelin.com](mailto:fabien.dufour@fr.michelin.com) (F. Dufour), [s.pigeot.remy@gmail.com](mailto:s.pigeot.remy@gmail.com) (S. Pigeot-Remy), [olivier.durupthy@upmc.fr](mailto:olivier.durupthy@upmc.fr) (O. Durupthy), [sophie.cassaignon@upmc.fr](mailto:sophie.cassaignon@upmc.fr) (S. Cassaignon), [valerie.ruaux@ensiacaen.fr](mailto:valerie.ruaux@ensiacaen.fr) (V. Ruaux), [stephane.torelli@cea.fr](mailto:stephane.torelli@cea.fr) (S. Torelli), [laurence.mariey@uniacaen.fr](mailto:laurence.mariey@uniacaen.fr) (L. Mariey), [francoise.mauge@ensiacaen.fr](mailto:francoise.mauge@ensiacaen.fr) (F. Maugé), [corinne.chaneac@upmc.fr](mailto:corinne.chaneac@upmc.fr) (C. Chanéac).

<sup>1</sup> Present address: Michelin, CT de Ladoux, Rue Bleue, ZI Ladoux, 63118 Cebazat, France.

<sup>2</sup> Present address: Ahlstrom Group Product & Technology Development, Ahlstrom Research and Service, ZI de l'Abbaye, Impasse Louis Champin, 38780 Pont-Evêque, France.

influence of the exposed crystallographic faces, and thus the influence of the particles morphology, on the photocatalytic properties remains unclear [10].

The photocatalytic degradation of a pollutant is a multi-step process in which the structural characteristics of the materials may impact differently. Indeed, electrons and holes must first be efficiently photogenerated within the bulk material and migrate to the surface where they are likely to react. The anatase structure is efficient in producing those charge carriers but their surface or bulk recombination and their surface trapping may depend on the crystalline quality and the particles shape [11]. In a second step, surface reactions involving those charge carriers may proceed directly with the pollutant very close to the surface or with intermediate molecules such as water or solubilized oxygen to yield active radicals that are prone to degrade pollutants near to the surface. Again, the relative reactivity of the exposed surfaces impacts the global efficiency of the photocatalytic material.

The aim of the present study is to provide a detailed correlation between the photocatalytic efficiency of different anatase morphologies on the same photocatalytic test and their surface characteristics. Sol-gel syntheses [12,13] were used to prepare pure anatase nanoparticles with a good structural and morphological control. The focus was led on particles synthesized in water as reacting medium. The rhodamine B degradation was chosen as photocatalytic test in the present study since it is easy to handle and commonly used in the literature as a tracer dye. In addition, it may involve direct surface reactions. The photocatalytic efficiencies of the different  $\text{TiO}_2$  morphologies for that specific pollutant may either be correlated to their ability to avoid recombination of photogenerated charge carriers, to produce active surface radicals or to directly transfer holes on the adsorbed dye. On that last point the adsorption efficiency may be understood in terms of the interaction of Lewis/Brønsted surface acidic sites with the corresponding basic sites of the dye.

In order to elucidate the real impact of morphology, a fine characterization of four anatase particles morphologies was achieved using high-resolution transmission electron microscopy analyses. The photocatalytic efficiencies of the selected samples for the degradation of the rhodamine B dye under UV light are presented. The surface reactivity was studied by a surface study by *in situ* Fourier transformation spectroscopy (FT-IR) using pyridine as basic probe and trough electronic paramagnetic resonance (EPR) for the detection of photogenerated radicals. The influence of the surface properties on the degradation of rhodamine B is rationalized.

## 2. Experimental

All chemicals were analytic grade reagents used without further purification (the oleic acid from Sigma is at 90%<sub>w</sub> purity). As a reference, P25 nanoparticles from Evonik were used as received.

### 2.1. Syntheses

#### 2.1.1. $A\mu W$

The synthesis is reported in details in one of our previous work [14]. A  $\text{Ti}^{4+}$  stock solution ( $[\text{Ti}^{IV}] = 1.0 \text{ mol L}^{-1}$ ) was prepared by dilution of the  $\text{TiCl}_4$  precursor in a  $\text{HCl}$  ( $3 \text{ mol L}^{-1}$ ) solution. Then, 30 mL of the stock solution were introduced into 100 mL of Milli-Q water; the pH of the solution was set to 6 with sodium hydroxide and the volume of the sample was completed to 300 mL with water. A white precipitate immediately appeared and aliquots of this suspension were transferred to Teflon cups, sealed in autoclaves and placed at 200 °C in a microwave oven (Synthos3000, Anton Paar) for 2 h.

#### 2.1.2. $AGlu$

The synthesis adapted from the procedure reported by Durupthy et al. is similar to the previous one [15] except that 1.98 g of glutamic acid (GA) was introduced under stirring into the reacting medium in order to obtain a  $[\text{GA}]/[\text{Ti}]$  ratio of 0.5 and the pH of the solution was then set to 4. A white precipitate immediately appeared and aliquots of this suspension were heated in a closed glass vessel at 120 °C in an oven for 48 h.

#### 2.1.3. $ARods$

The synthesis of  $\text{TiO}_2$  nanorods was adapted from Sugimoto [16]. Titanium isopropoxide (TIPO, 6.9 mL) was mixed with triethanolamine (TEOA, 6.7 mL) under stirring in a closed flask and the volume was completed to 30 mL with deionized water. Then, 1.4 mL of ethylenediamine was added. The measured pH was close to 10. Finally, water was added under stirring to complete the volume to 100 mL. A first aging-step, leading to the formation of a gel, was carried out by heating the closed flasks in an oven at 100 °C for 24 h. The resulting gel was poured into Teflon-lined autoclaves for a second aging step at 140 °C for 72 h.

#### 2.1.4. $ACubes$

The synthesis of anatase cube-shaped nanoparticles was adapted from Sugimoto [16]. TIPO (21.0 mL) was mixed with TEOA (20.3 mL) under stirring and the resulting solution was completed to 150 mL with water. 2.8 g of oleic acid previously added in 50 mL of water was mixed with the 150 mL of stock solution under constant stirring. A further addition of 50 mL of water was then supplied. The pH of the solution was found to be close to 10.5 and was adjusted if necessary to this value with  $\text{HClO}_4$  or  $\text{NaOH}$  solutions. Finally, water was added up to a volume of 300 mL. A first aging-step, leading to gel formation, was carried out by heating the closed flask in an oven at 100 °C for 24 h. The resulting gel was poured into Teflon-lined autoclaves for a second aging-step at 140 °C for 72 h.

The resultant precipitates of the whole as-synthesized oxide materials were collected by centrifugation, washed first with water, then with nitric acid ( $3 \text{ mol L}^{-1}$ ) and one last time with water. The obtained powders were then centrifuged and dried under a dry air-flow overnight. All the centrifugation steps are performed at 29 000 RCF during 20 min.

## 2.2. Characterization

### 2.2.1. X-ray diffraction (XRD) measurements

The phase and crystallite size analyses of  $\text{TiO}_2$  powders were performed with a Bruker D8 X-ray diffractometer operating in the Brag-Brentano reflection mode equipped with a nickel filter to select the  $\text{Cu}-\text{K}\alpha$  radiation. The data were collected in the  $2\theta = 10\text{--}70^\circ$  range with  $0.05^\circ$  steps. Pattern analyses were performed using EVA software (Bruker AXS) and the ICDD DD View PDF-4 + 2009 RDB base (PDF number 00-021-1272 for anatase, 00-021-1276 for rutile and 04-007-0758 for brookite). The proportions of the different  $\text{TiO}_2$  polymorphs were assessed from the relative areas of the anatase (101), brookite (121) and rutile (110) diffraction lines obtained after diagram deconvolution and according to the procedure reported in Pottier et al. [17]. For average size of anatase nanoparticles, (101), (004) and (200) diffraction lines were exploited as reported elsewhere [14]. In terms of particle size measurements, the evaluated error is  $\pm 0.5 \text{ nm}$ .

### 2.2.2. Transmission electron microscopy

The morphology and mean particle size of the samples were analysed by transmission electron microscopy (TEM) using a Tecnai spirit G2 apparatus operating at 120 kV ( $\text{LaB}_6$ ). High resolution TEM (HRTEM) was performed at 200 kV on a Jeol-Jem 2011HR apparatus

(LaB<sub>6</sub>). For the size distributions, more than 100 TiO<sub>2</sub> particles for each sample have been measured.

### 2.2.3. Specific area measurements and thermogravimetric analyses

The specific surface area measurements were carried out by nitrogen adsorption at 77 K using a Belsorb Max instrument. Prior to measurements, all TiO<sub>2</sub> powders were degassed under a primary vacuum at 150 °C overnight using a Belprep II instrument. The BET method was applied to determine the specific area. TGA experiments were carried on a Netzsch STA 409 device to determine the water and organic content of the powders.

### 2.2.4. Photocatalytic experiments

All tests were carried out in an open cylindrical reactor. A volume of 100 mL of rhodamine B (RhB) solution with an initial absorbance of 2.38 at  $\lambda = 555$  nm was mixed with 0.1 g (photocatalyst load of 1.0 g L<sup>-1</sup>) of the studied powder. UV radiation exposures were performed using a Philips PL-L mercury lamp (18 W), emitting UV-A radiation with a peak emission at 365 nm. The lamp spectrum is reported in Fig. SI-A. The total radiance intensity in the suspension, of 1.7 mW/cm<sup>2</sup>, was measured with a digital radiometer (VL-3W, UVItec). Prior to UV exposure, the aqueous suspension was magnetically stirred in the dark for 30 min to ensure the adsorption equilibrium. Aliquots of 2 mL were withdrawn at different irradiation times (5, 10, 15, 25, 40 and 60 min) and centrifuged to remove TiO<sub>2</sub> particles during 30 min at 22 000 RCF. The supernatants were analyzed by visible spectrophotometry in the 450–650 nm range using a Cary5000 spectrometer from Agilent Technologies. No significant shift of the RhB peak at 555 nm was observed and, consequently, the peak intensity at this wavelength was used for the degradation study (except for the ACubes sample, see below).

### 2.2.5. Optical band gaps

UV-visible diffuse reflectance spectra (DRS) of the samples were recorded on a Cary 5000 spectrometer with integrating sphere from 300 to 800 nm. For a crystalline semiconductor with an indirect gap, the optical absorption near the band edge is expressed by the formula  $\alpha h\nu = A(h\nu - E_g)^2$ , where  $\alpha$ ,  $h$ ,  $\nu$ ,  $E_g$  and  $A$  correspond to the absorption coefficient, Planck constant, light frequency, band gap and a constant, respectively. The band gap is thus estimated on the plot  $(Ah\nu)^2 = f(h\nu)$  by intercepting the tangent of the plot with the abscissa axis.

### 2.2.6. Fourier Transformation Infrared spectroscopy (FT-IR)

The surface groups and the acidity of the TiO<sub>2</sub> nanoparticles were studied by FT-IR using pyridine as a basic spectroscopic probe. Infrared spectra were recorded on self-supported discs ( $\sim 2$  cm<sup>2</sup>, i.e.  $\sim 20$  mg) which were placed into an infrared quartz cell equipped with KBr windows connected to a vacuum line. The FT-IR spectrophotometer was a Nicolet Nexus apparatus equipped with an extended KBr beam splitter and a mercury cadmium telluride detector (resolution of 4 cm<sup>-1</sup>). Spectra were recorded at room temperature from 4000 to 400 cm<sup>-1</sup> from the accumulation of 256 scans with a step of 1 cm<sup>-1</sup> (analogical resolution of 0.5 cm<sup>-1</sup>). Prior to the adsorption experiment, samples were activated by heating (3 °C min<sup>-1</sup>) to 200 °C under secondary vacuum ( $P \sim 10^{-4}$  Pa) and kept at this temperature for 2 h. After the activation (first recorded spectrum  $d_0$ ), pyridine was introduced into the cell via the vacuum line at equilibrium pressure (133 Pa). Pyridine (Aldrich, >99% grade) was dried on molecular sieves prior to its use. A second spectrum  $d_1$  is recorded at 20 °C. The adsorbed pyridine was then evacuated under primary vacuum ( $10^{-3}$  Pa,  $d_2$  spectrum), secondary vacuum ( $10^{-4}$  Pa,  $d_3$  spectrum) and at increasing temperature under

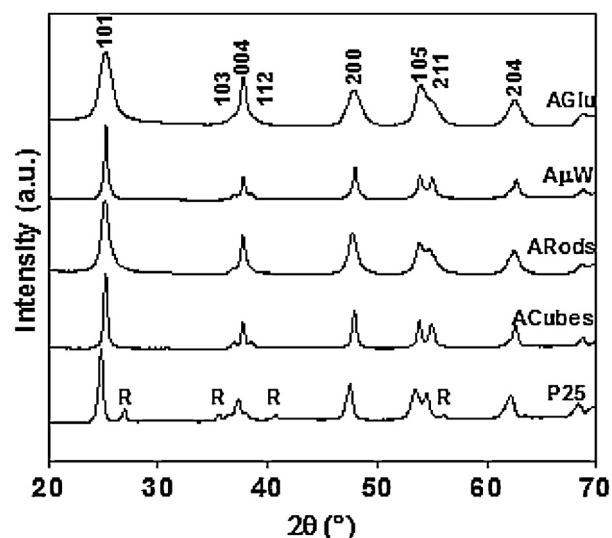


**Fig. 1.** XRD powder patterns of the synthesized particles and of the reference materials P25. The anatase peaks are indexed on the AGlu pattern and the rutile peaks are indicated with "R" on the P25 sample.

secondary vacuum (50 °C for  $d_4$ , 100 °C for  $d_5$ , 150 °C for  $d_6$  and finally 200 °C for  $d_7$ ).

### 2.2.7. Electronic paramagnetic resonance.

3 mg of TiO<sub>2</sub> powders were dispersed in 2 mL of milliQ water. After 10 min of equilibrium time in the dark, the suspension is irradiated two minutes under vigorous stirring. UV radiation exposures were performed using the same lamp as for photocatalytic experiments. The total radiance intensity in the suspension, of 1.7 mW/cm<sup>2</sup>, was measured with a digital radiometer (VL-3W, UVItec). Then, 1 mL of a freshly prepared 0.1 mol L<sup>-1</sup> DMPO solution is added (final concentrations of 1 g L<sup>-1</sup> of TiO<sub>2</sub> and 0.02 mol L<sup>-1</sup> of DMPO). Few microliters are withdrawn at selected times with a quartz capillary (10 μL from Hirschmann Laborgeräte), which is then immediately closed to the lower extremity and place in an EPR quartz tube and is finally put into the spectrometer cavity. Due to the fast degradation kinetics of adducts the timing of each preparation step from the solution preparation to the spectra measurements was strictly controlled for all the samples. The spectra were recorded at 22 °C on a Bruker EMX EPR spectrometer. The following instrument settings were used: microwave power 20 mW, microwave frequency 9.75 GHz, modulation frequency 100 kHz, modulation amplitude 2 G, conversion time 40.96 ms (constant time 10.24 s), sweep time 42 s, resolution 1024, 2 scans. The obtained spectra are reported after baseline correction with the Bruker WIN-EPR program, which was then used to calculate the normalized double integration used to perform a quantitative comparison among the samples.

## 3. Results and discussion

### 3.1. Detailed nanoparticles characterizations

The anatase purity of all synthesized samples was checked on the XRD patterns reported in Fig. 1 and confirmed by Raman spectroscopy (Fig. SI-B). The diffractograms of the different samples only differ on the relative intensity and broadness of the peaks which are closely related to the size and shape of nanoparticles. For TiO<sub>2</sub> P25, additional diffraction peaks corresponding to the rutile phase were observed (anatase 80%, rutile 20%).

The usual morphology of TiO<sub>2</sub> anatase macrocrystals found in mineralogy is a truncated square bipyramid exposing mainly

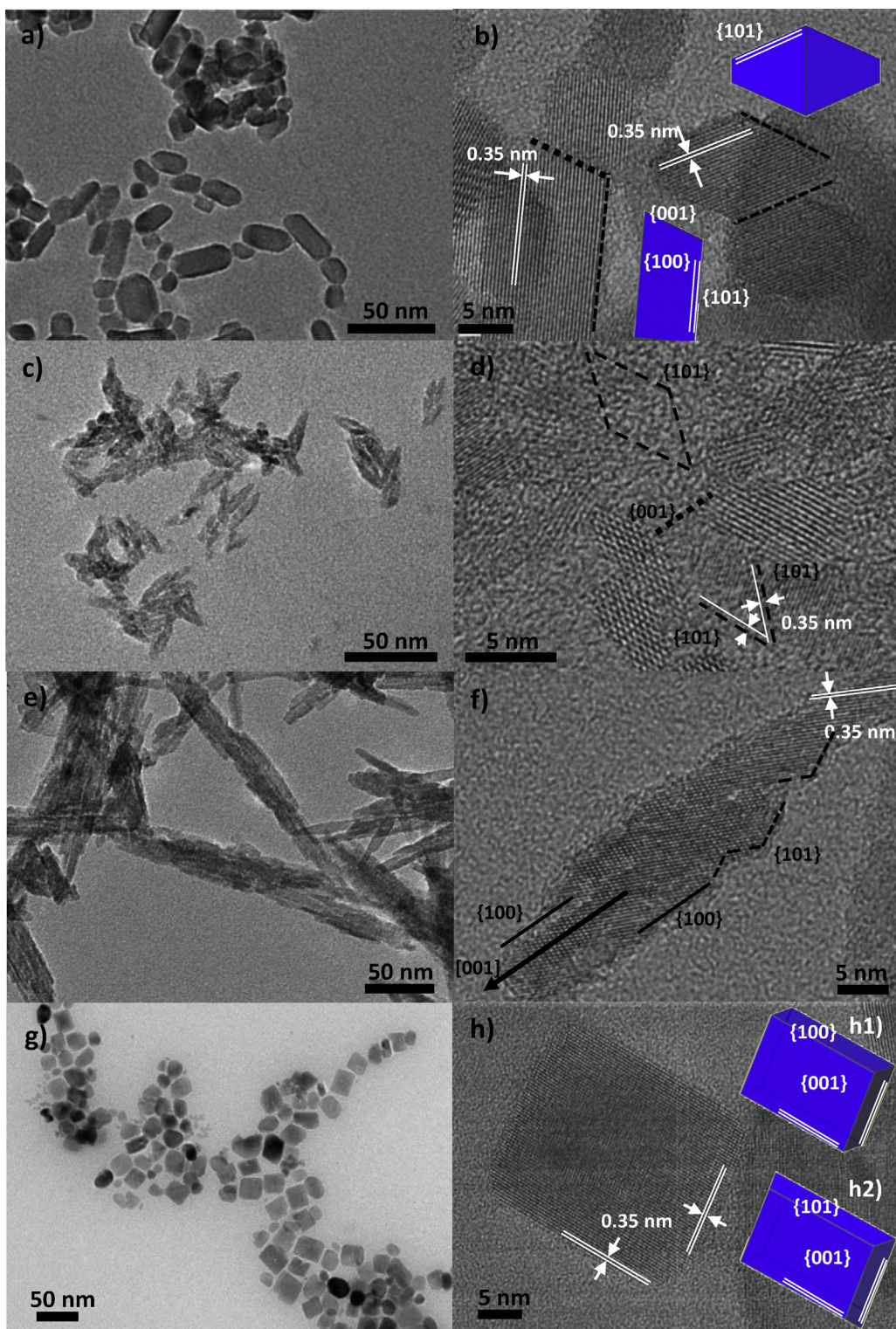


**Fig. 2.** TEM and HRTEM images of (a and b)  $\text{Ap.W}$ , (c and d)  $\text{AGlu}$  (e and f)  $\text{ARods}$  and (g and h)  $\text{ACubes}$  samples. Measured distances between lattice fringes are attributed to the  $\{101\}$  anatase planes. Blue polyhedrons presented in selected HRTEM images represent 3D objects that may account for the 2D HRTEM image. Lateral faces of the particles corresponding to  $\{100\}$  planes are shown with plain lines, those corresponding to  $\{100\}$  planes are shown with dashed lines and those corresponding to  $\{001\}$  planes are shown with dotted lines. (For interpretation of the references to color in this figure legend, the reader is referred to the web version of this article.)

the  $\{101\}$  faces and lower amounts of  $\{001\}$  as top faces. It corresponds to the morphology obtained by the Gibbs–Wulf construction [18]. Indeed, the most stable face of the anatase structure is the  $\{101\}$  face [19]. At the nanometer scale, the hydrolysis in water of the  $\text{TiCl}_4$  precursor and a gentle heating gives the same morphology [14]. The versatility of the sol–gel process allows

to change the particle morphology and for instance the relative amount of the  $\{101\}$  and  $\{001\}$  exposed faces and also to display additional faces that are hardly observed in macro crystals. For each synthesized samples, TEM (see Fig. 2) and XRD analyses were combined to determine the anatase particles shape and the nature of exposed faces. Details of the statistical study of the

**Table 1**

Structural, morphological and optical properties of the studied samples.

Samples	A $\mu$ W	AGlu	ARods	ACubes	P25
Structure	A	A	A	A	4/5 A, 1/5 R
Size (nm)	24	14	20	24	25
Mainly exposed faces	{101} {100}	{101}	{101} {100}	{001} {100} {101}	—
Specific area ( $m^2 g^{-1}$ )	120	190	120	70	50
Optical gap (eV)	3.21	3.13	3.18	3.14	3.08

different samples dimensions and shapes are reported in supplementary information (Fig. SI-C).

The TEM and HRTEM images of the A $\mu$ W sample reported in Fig. 2a and b shows nanorods ( $8 \times 24$  nm) with an anisotropy ratio of about 3 (determined as the ratio  $d_{[001]}/d_{[100]}$ ) as the most observed shape. HRTEM pictures show that the lateral faces of these rods are a combination of {101} and {100} faces and thus the elongation axis is not [001], as usually obtained for anisotropic anatase particles [20–23]. The top faces could not easily be assigned, being either {101} or {001} faces depending on the studied particle. The secondary morphology observed (>20%) is the truncated square bipyramid exposing mainly {101} faces.

The use of glutamic acid as organic additive led to pure anatase phase (AGlu sample) presenting elongated bipyramid morphology as shown in Fig. 2c and d and confirmed from the XRD peaks fitting. The lattices fringes observed in the HRTEM images confirm that the sides of the bipyramids are {101} faces. The anisotropy ratio is about 2.4 ( $5 \times 12$  nm) close to the ratio of a perfect bipyramid. Few {001} faces are expected, as observed on the TEM pictures. However, some of the smallest crystallites still exhibited {001} faces and defaults such as {101} steps as shown in Fig. 2d.

The two procedures, inspired by the work of Sugimoto [16] also use organic additives. First a gel is formed from heating a solution of titanium isopropoxyde and TEOA at pH 10–11. A second aging step of the gel at higher temperature induces the crystallization of different original morphologies depending on the pH fixed and the presence of a selected additive.

In the presence of ethylenediamine, rod-like sample with a 200 nm length were obtained as shown in Fig. 2e and f. The XRD pattern fit of that sample labeled ARods gave crystallites size of 20 nm along the [001] direction and around 10 nm in the other directions. The differences with TEM measurements are explained by the polycrystallinity of these particles. The nanorods are composed of the oriented aggregation of several smaller monocristalline rods, stacked along the [001] axis. With such a large anisotropy along the [001] direction, the presence of {100} faces as lateral surfaces of the rods is expected (see Fig. 2f). Yet the HRTEM pictures reveal that a significant part of these lateral faces are also made of {101} steps. The presence of {101} faces on the lateral faces of the rods could be either attributed to the enhanced washing steps, to the specific adsorption of the ligands or to the formation pathway of the rods [24].

In the last sample, oleic acid was used as shape controller and the obtained particles were labeled ACubes for the TEM pictures displaying pseudo-cubic nanoparticles (25 nm) as shown in Fig. 2g and h. According to the tetragonal symmetry of the anatase structure, perfect cubes can be obtained with both {100} and {001} faces. A thorough study of the HRTEM pictures shows that in addition to those faces, few amounts of {101} faces cannot be excluded (Fig. 2h, inset h1 and h2). Snapshots from a tomography movie reported in Fig. SI-C show that the same particle may present a square projection in a selected orientation in agreement with the cubic shape and a more ovoid projection after a 60° rotation. All the exposed surfaces could not be unambiguously indexed, especially for the ovoid shapes, where higher Miller index faces could be

exposed. This indicates that there may be less {001} faces exposed than initially expected. The {001} face is very reactive and tends to reconstruct under harsh conditions such as vacuum [25]. The intensive washing of the anatase particles may have damaged them. TEM picture of the ACubes sample with a softer washing are report in Fig. SI-D: the particles are clearly closer to perfect cubes. Yet even with the thorough washing, residual organic molecules are still adsorbed in that sample as confirmed by the slight yellow color of the powder and the difficulty to disperse it in water.

Thus, these four anatase nanoparticles morphologies present a variety of exposed faces from extended {101} surfaces (square bipyramids) and stepped {101} (rods) to a combination of {100} and either {101} (A $\mu$ W) or {001} (cubes).

As for TiO<sub>2</sub> P25 composed of both anatase (80%) and rutile (20%) phases, the nature of exposed surfaces is more complex and is studied in detail in the literature by HRTEM with selective dissolution of either anatase or rutile component [26–29]. The anatase nanoparticles seem to expose mainly the {101} faces and often present truncated bipyramids.

The optical gaps and specific areas of all the samples are also reported in Table 1. The light absorption behaviors of all the studied samples are rather similar. On the contrary, the specific surfaces of the synthesized samples vary from 70  $m^2 g^{-1}$  (ACubes) to 190  $m^2 g^{-1}$  (AGlu) and the P25 sample displays the lowest specific area. The differences in surface area are correlated to the different crystallite sizes. This may have consequences on the confinement of photogenerated charge carriers, on the recombination behavior and consequently on the photocatalytic activity [30–33]. The crystalline quality of the nanoparticles may also impact on that recombination rate [34,35]. In order to ensure that the differences of confinement effect and crystalline quality are not the predominant parameters that impact photocatalytic properties the chosen syntheses are all performed in a similar temperature range (120–200 °C). Time resolved microwave conductivity experiments [14] were also performed (not shown) and, besides the P25 sample, all the synthesized samples present roughly the same photo conversion efficiency and recombination rate. This specific point will be discussed in a future publication.

The organic contents calculated from TGA analyses are 6, 7 and 5 wt% for AGlu, ARods and ACubes, respectively. This corresponds roughly to 1 organic molecule/nm<sup>2</sup>. Since the area of a carboxylate surface group (in oleic acid for instance) is about 0.2 nm<sup>2</sup> this means that a maximum surface coverage of 20% with organic residues may block the TiO<sub>2</sub> reactive surface sites. The ACubes sample is, *a priori*, the more passivated sample with the smaller surface area but is still able to adsorb more rhodamine B dyes at its surface than the other samples as discussed below. The impact of organic residues on the different samples was not studied here more precisely.

### 3.2. Photocatalytic efficiencies

The experimental conditions of the photocatalytic test were carefully defined to be reliable, comparable with several studies found in literature and are briefly discussed below. The choice of the RhB as a dye molecule was done because it allows an easy and

**Table 2**

RhB relative adsorption after 30 min equilibrium in dark and initial degradation rates.

TiO <sub>2</sub> samples	A $\mu$ W	AGlu	ARods	ACubes	P25
RhB adsorption	10%	13%	15%	20%	10%
Initial degradation rate (mmol L <sup>-1</sup> min <sup>-1</sup> )	69	37	29	9	65
t <sub>95%degrad.</sub> (min)	50	25	40	–	50

fast monitoring of its degradation by visible spectroscopy and its quantitative adsorption on the photocatalyst may impact the photodegradation [37]. However, it is not the perfect model pollutant since it absorbs photons in the visible range and this absorption may induce a photosensitization mechanism that can infer on the true photocatalytic process. A study more focused on the comparison of different model pollutant on the same photocatalyst is on preparation to address more specifically that point [38]. The photocatalysis test consists first in the dye adsorption equilibrium in the dark and then in the partial or complete dye degradation under UV irradiation. Preliminary experiments showed that no catalytic or self-degradation of the RhB was possible without light irradiation exposure and thus the first step only corresponds to the adsorption equilibrium. Unless for cubes, no significant shift of the RhB maximum absorption was observed and no sub-products absorbing in the 450–650 nm range were observed. This indicates that the sensitized-degradation of RhB via N-deethylation process can be neglected. The RhB concentration and photocatalyst load (1.0 g L<sup>-1</sup>) were chosen in order to observe a complete degradation of the dye within one hour with P25. The suspension concentration of 1.0 g L<sup>-1</sup> also corresponds to the maximum of photon absorption [39,40]. The choice of the iso-weight rather than iso-surface test was done to match with the industrial point of view that the price of the photocatalyst is defined per kilogram of product. Moreover, the quality of the photocatalyst dispersion in water, which is also a key parameter in materials efficiency, is not directly linked to its specific surface measured on the dried solid. Indeed, with the lowest specific surface, the P25 photocatalyst presents the best dispersion state in water. The absorption spectra at different degradation time for the 5 photocatalysts are reported in Fig. SI-E and the extracted data are reported in the Table 2 and Fig. 3.

The photocatalytic efficiency of different materials may be compared on the same test either through the comparison of the initial degradation rate or through the time needed to degrade a set amount of pollutant. In the present case, the use of initial degradation rate reported in Table 2 gave the following order: P25 ~ A $\mu$ W > AGlu > ARods » ACubes. On the other hand, the time

needed to degrade 95% of the dye presents a different order: AGlu > ARods > P25 ~ A $\mu$ W » ACubes. The usual exponential like curve shape of the degradation kinetics are observed for P25 and A $\mu$ W samples. It is not the same for the other samples on which a competition during the first minutes of the test may take place between the degradation of the residual organic and that of the RhB. Indeed, the adsorbed organic impurities may partially block the access of the dye to the photocatalyst surface and may be degraded during the first minutes of the experiment instead of the targeted pollutant. The AGlu sample seems to be a promising photocatalytic material since 95% of RhB is degraded in 25 min against 50 min for P25. A more complete study of this sample is reported elsewhere [41].

In order to explain the photocatalytic efficiency differences between the four anatase morphologies, the properties specific to each surface of the samples were studied. The most efficient sample AGlu is exposing only the {101} faces. A $\mu$ W is slightly less efficient which may be due to a lower activity of the {100} faces than the {101} ones. The same goes for ARods which exhibit a behavior between AGlu and A $\mu$ W. The ARods sample shows the very importance of the surface nature exposed: with a very different size and shape compared to AGlu the nearly similar activity may be explained by the exposition in both cases of {101} faces. The efficiency of P25 is ranging after AGlu but at the same level at A $\mu$ W with no particularly overexpressed face. Finally, it could be surprising to see that ACubes, the sample exposing the largest part of {001} among the samples is the less efficient. Indeed, in literature {001} anatase face is *a priori* seen as a more active face than {101} [9,10,42].

A clear description of the active surface sites of each sample may then explain more precisely the observed differences in photocatalytic behavior. The focus was put more specifically on the acidic sites that are prone to adsorb the selected dye.

### 3.3. Surface dependent acidic sites

The changes in the nanoparticles morphology directly impact on the nature, number and reactivity of exposed surface groups, which means here the acidic properties in terms of Brønsted or Lewis acidity. Actually, the surface acidity of oxides and oxy-hydroxides is due to surface oxygen atoms that present less metallic neighbors than in the bulk. Consequently, the undercoordinated oxygen they may present a negative net charge and an ability to exchange protons with the solution. That Brønsted acidity depends on the number of metallic neighbors and their distance to the considered oxygen. As a defined structure (TiO<sub>2</sub> anatase here) is not truncated in the same way to form {101}, {001} or {100} surfaces, the number and lengths of remaining M–O bonds may differ between the different surfaces. A model proposed by Hiemstra et al. [43,44] may even propose pK<sub>a</sub> value for the different surface sites and it was already applied in our group on boehmite ( $\gamma$ -AlOOH) [45,46] and on bismuth tungstate (Bi<sub>2</sub>WO<sub>6</sub>) [47]. On the truncated metal oxide structures, undercoordinated metallic atoms may also be present at the surface and present a Lewis acidity that depends on the degree of undercoordination. It is well known for aluminum in aluminum oxides as well as in zeolites [48]. That is why the different morphologies of a same structure will interact differently with a basic molecular probe.

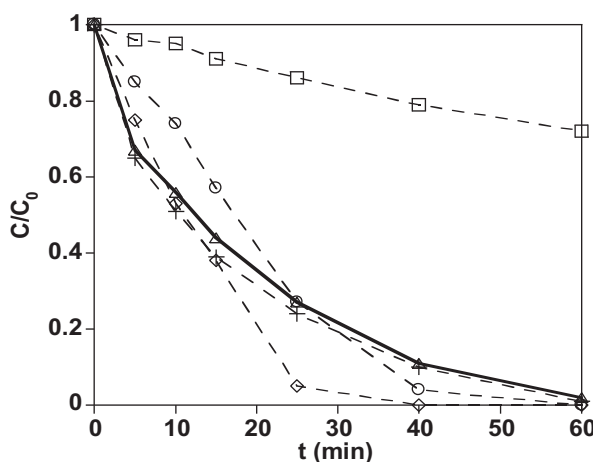


**Fig. 3.** Photocatalytic degradation curves of the RhB solution by the anatase samples (dotted lines and cross for A $\mu$ W, diamond for AGlu circle for ARods, square for ACubes) and the P25 reference (plain line and triangles).

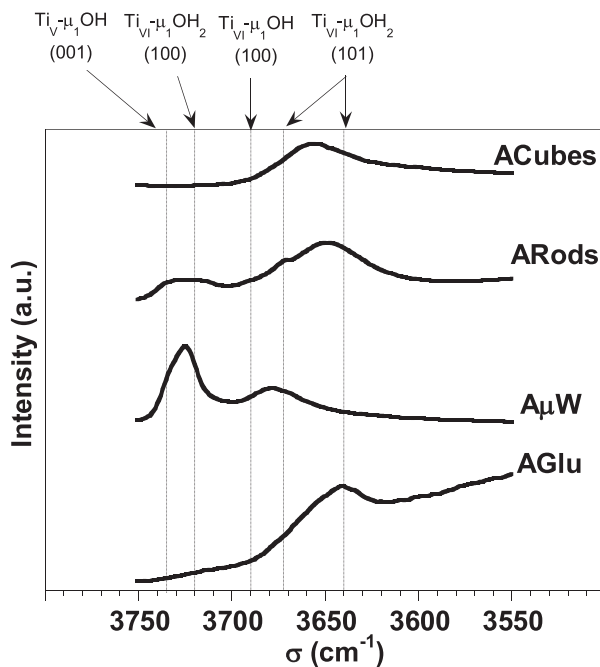


**Fig. 4.** FT-IR spectra after activation ( $d_0$ ) for the anatase samples. The attribution of the different surface OH vibrators is done according to [55].

The FT-IR spectroscopy is a technique that may provide accurate information on the composition and surface activity of  $\text{TiO}_2$  [49–52]. Indeed, IR signals corresponding to surface hydroxyl groups are very sensitive to their atomic vicinity and their evolution under different vacuum and temperature conditions were shown to be useful in understanding the evolution with sintering of  $\text{TiO}_2$  nanoparticles [53]. Moreover, molecular surface probes such as  $\text{NH}_3$ , [49]  $\text{CO}$  [53] and in the present case pyridine [54] interact with different reactive surface sites and thus produce different IR signals, allowing a precise description of the nanoparticles surface sites. It is all the more simple to analyze the data from IR spectra that the  $\text{TiO}_2$  nanoparticles used are well described and display a minimum of different exposed surfaces. That is why the IR signals acquired in the different experimental conditions for the 4 sets of particles could be faithfully described and compared. To allow quantitative comparisons, the reported peaks areas were balanced with the irradiated sample surface (the weight of the disk is multiplied by the specific area of the sample). Most of the conclusions proposed on the comparison of the obtained FTIR spectra remains however qualitative.

The signature of the OH bonds is observed in the range of  $3300\text{--}3800\text{ cm}^{-1}$  in the  $d_0$  spectra just after activation as reported in Fig. 4. In this range, the wavenumbers of O–H vibrations depend first on the nature of the adsorption vibrator on the surface: it may either correspond to water molecules physisorbed/chemisorbed on the surface or to hydroxyl surface groups. More precisely, the atomic topology of the surface on which the OH group is adsorbed impacts the measured wavenumber. This was first demonstrated by Dzwigaj et al. in a study combining FTIR spectroscopy and DFT calculation on two sets of different anatase nanoparticles [55]. The correlation between specific OH vibrators and a define surface is not based in this study only on experimental results such as grazing angle FTIR on monocrystalline surfaces but the differences in oscillator frequency calculations on the different model surfaces can be considered as reliable. The same approach was successfully used to distinguish the OH groups of a defective  $\text{MgO}$  surface [56].

In the  $\text{A}\mu\text{W}$  sample the signal attributed to physisorbed water molecules is relatively weak indicating a good removal for these

temperature (2 h at  $200^\circ\text{C}$ ) and pressure conditions ( $10^{-4}\text{ Pa}$ ). The two observed bands in the  $3600\text{--}3750\text{ cm}^{-1}$  range could be correlated to the two faces exposed on that sample: the strongest band around  $3675\text{ cm}^{-1}$  corresponds mainly to  $\{101\}$  surfaces and the smaller band around  $3725\text{ cm}^{-1}$  to  $\{100\}$  planes according the attribution proposed by Dzwigaj et al. [55] On the second band a shoulder at higher wavenumber values is observed and may be attributed to the small contribution of hydroxyl groups on the  $\{001\}$  faces (forming the tops of the rods). From that deconvolution we may state that the  $\text{A}\mu\text{W}$  display significant amount of  $\{100\}$  faces. On the spectrum of the  $\text{AGlu}$  sample, the OH vibration band corresponding to  $\{101\}$  faces is also observed but it is broader and shifted to  $3640\text{ cm}^{-1}$ . Actually, that value is also reported to correspond to a  $\text{Ti}_{\text{VI}}-\mu_1\text{OH}_2$  surface group of  $\{101\}$ . This difference may be explained by the impact of remaining physisorbed water molecules (very broad peak centered at  $3200\text{ cm}^{-1}$ ) and glutamic acid (different thin peaks in the  $1200\text{--}1700\text{ cm}^{-1}$  range) on the OH oscillators. Indeed, the formation of H bond network with additional water molecules or carboxylate/amine groups of the amino acid implies a relative OH bond elongation and consequently less energetic vibration. The OH region of the  $\text{ARods}$  sample, looks like a composite of the two precedently described spectra: one band centered at  $3650\text{ cm}^{-1}$  with a shoulder at  $3670\text{ cm}^{-1}$  (2.8 a.u.) corresponds to the  $\{101\}$  faces and another broad and flat band close to  $3730\text{ cm}^{-1}$  corresponding to the  $\{100\}$ , the ratio between the first and the second band being about 3. This means that relatively more  $\{101\}$  faces are present in the  $\text{ARods}$  sample than in the  $\text{A}\mu\text{W}$  one, which confirms that  $\text{ARods}$  actually presents mainly  $\{101\}$  steps along the lateral faces of the rods rather than the expected  $\{100\}$ . The shift in position of the IR band corresponding to OH groups on  $\{101\}$  surfaces may again be attributed to the presence of physisorbed water and unwashed ED and TEOA molecules. The  $\text{ACubes}$  sample presents only one broad band centered on  $3650\text{ cm}^{-1}$  corresponding *a priori* to  $\{101\}$  surfaces. This sample also presents strong bands corresponding to oleic acid (bands in  $1200\text{--}1700\text{ cm}^{-1}$  and  $2800\text{--}3000\text{ cm}^{-1}$  regions see Fig. SI-F) and water molecules still adsorbed. This OH groups surface attribution disagrees with results from the TEM and XRD studies where  $\{100\}$  and  $\{001\}$  surfaces are mainly proposed. From the analysis of this OH vibration region, a good correlation between the IR band positions and the faces attribution is observed despite the presence of few organic residuals. The specific case of the  $\text{ACubes}$  sample is discussed later.

The adsorption of a basic probe and its temperature controlled desorption was then analyzed to compare acidic surface properties of all samples. Pyridine is commonly used to obtain information about the surface acidic sites of the particles: the different vibration modes of the molecule are altered by the nature of its adsorption site [49,52,54,57,58]. The overlapping of certain vibration modes with the characteristics bands of remaining organic impurities had us select specific zone discussed below that are representative of the different adsorption modes namely chemisorption on the Lewis acidic sites, on the Brønsted sites and the physisorption. For sake of conciseness, only one region corresponding to Lewis acidity is reported here; the discussion on the other two kinds of sites is reported in Fig. SI-G and H and only the conclusions are presented.

A commonly studied band in the literature for the characterization of Lewis sites is the  $\nu_{8a}$  band located around  $1585\text{--}1615\text{ cm}^{-1}$  because its position is known to shift toward higher wavenumber with increased site acidity [59]. The thermodesorption behavior of the band is also correlated to the strength of the site. Unfortunately, organic remaining in some of our samples cannot be simply treated by a simple base line correction because they were found to desorb at the same time as pyridine. In order to avoid the influence of organic residues, the  $\nu_{12}$  vibration mode of the Lewis acidic

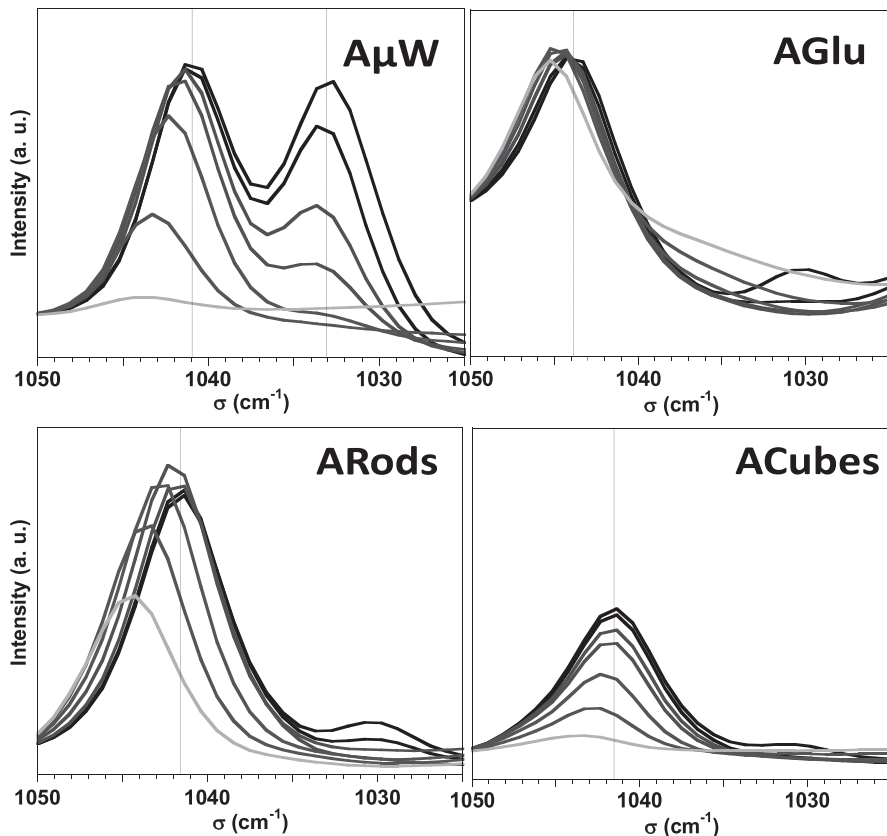


**Fig. 5.** Selected region of the FT-IR spectra corresponding to the  $\nu_{12}$  pyridine vibration mode and its thermodesorption behavior (from black  $d_1$  to light gray  $d_7$ ) for the different samples: vertical dotted lines correspond to the positions of the stronger vibration bands just after pyridine adsorption ( $d_0$  see Section 2).

sites around  $1040\text{ cm}^{-1}$  in wavenumber which can be correlated to the  $\nu_{8a}$  band was chosen for comparative analysis [60]. On the A $\mu$ W sample, the pyridine adsorbed on Lewis sites is totally desorbed at  $200^\circ\text{C}$  and the band is shifted from  $1041.0\text{ cm}^{-1}$  just after adsorption to  $1043.3\text{ cm}^{-1}$  at  $150^\circ\text{C}$  as reported in Fig. 5. In addition to that strong band, a second band specific to the A $\mu$ W sample is observed at  $1033\text{ cm}^{-1}$  and disappears below  $50^\circ\text{C}$  of heating treatment. This indicates a less acidic behavior of these sites compared to the previous ones. The AGlu sample presents a strong adsorption of pyridine on Lewis acid sites for the area of the band is approximately twice that of the A $\mu$ W sample (for a same sample surface), the band maximum is shifted from  $1043.9$  to  $1045.2\text{ cm}^{-1}$  with increased desorption temperature and about 75% of initially adsorbed pyridine is still present at  $200^\circ\text{C}$ . This confirms that the AGlu sample is a much more acidic sample than A $\mu$ W. So is in a less extent the ARods sample: the amount of adsorbed pyridine is about the same as AGlu the band maximum is shifted from  $1041.6$  to  $1043.5\text{ cm}^{-1}$  with temperature and about 70% of the pyridine is retained at  $200^\circ\text{C}$ . This is consistent with the fact that both samples exhibit mainly the {101} faces. The slightly lower wavenumber values may be explained by the presence of more defects on the ARods surfaces. For a normalized exposed surface, the ACubes sample pyridine initially adsorbed in that region represents only 60% of that on AGlu and it is nearly totally desorbed at  $200^\circ\text{C}$ . The band maximum observed at  $150^\circ\text{C}$  is  $1042.8\text{ cm}^{-1}$  while it is at  $1041.5\text{ cm}^{-1}$  just after adsorption. These values show that ACubes is the less acidic sample for the Lewis sites. It is almost the same as the A $\mu$ W sample but the second weaker acidity in ACubes is hardly observed at  $1033\text{ cm}^{-1}$ . This second band is also hardly observed for the AGlu and ARods samples, and it disappears with improved vacuum treatment indicating weak Lewis acidity.

Finally, most of the acidic sites observed on the different morphologies and discussed were Lewis sites except for AGlu sample where relatively strong Brønsted and physisorption sites were also detected. However, the Lewis acidic sites observed in gas phase using pyridine as a probe may have vanished or have been converted into other kinds of acidic sites when considering the same photocatalyst in solution during the degradation test. Thus, the FT-IR characterization approach does not provide straightforward information on the adsorption mode of the RhB but rather informs about the overall acidity of the samples. From the different analyzed regions of the FT-IR spectra, a good correlation can be found with the morphologies deduced from TEM and XRD characterizations and interesting insights on the samples acidity can be proposed.

In order to relate the diversity of the acidic properties of the anatase samples with the RhB photodegradation efficiency, a closer look to the degradation process must be done. As stated earlier, one of the key points for the degradation of a pollutant is the quality of the interaction with the photocatalyst surface. This is even more crucial when dealing with degradation mechanisms that directly involve surface trapped electrons or holes transfer. It must be noticed here that the  $1\text{ g L}^{-1}$  samples suspensions pH are  $3.2\text{--}3.4$  for all samples except for the P25 with a pH of 4.3. This may be explained by the last but one washing step with nitric acid that implies a surface protonation and the resuspension of the powder acidify the dye solution. In the present experimental conditions the titania surface charge is slightly positively charged as determined elsewhere on those samples [61]. In that pH range, RhB is also positively charged and electrostatic interactions are consequently excluded. However, both an adsorption of the RhB dye with the carboxylate group or with the lone pair of amino groups is possible. Since in most systems no N-deethylation is observed, it is

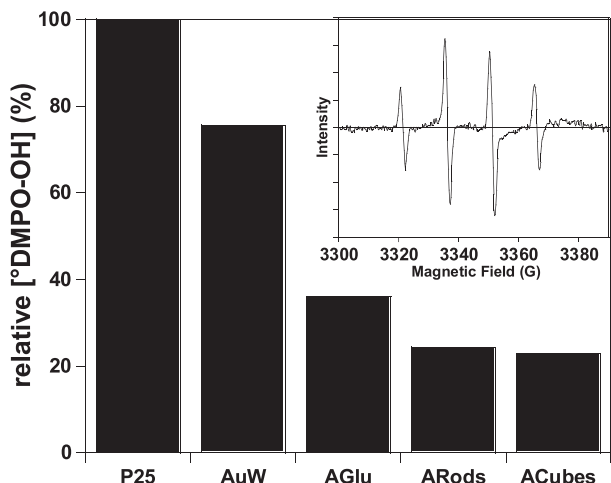


**Fig. 6.** Relative  $\cdot\text{DMPO}-\text{OH}$  production (referred to the adduct concentration for P25) of the studied samples. Inset: EPR spectrum of the  $\cdot\text{DMPO}-\text{OH}$  spin adduct of the P25 sample (measured  $a_N = a_H = 15.0$  for 15.05 theoretically) [65].

possible that the carboxylate group of the dye is adsorbed on the acidic sites of the samples. The good photocatalyst efficiency of the AGlu sample toward RhB degradation, even better than the P25 reference, may then be attributed to the larger number of surface acidic sites and their higher strength. This correlation was proposed for the same dye on bismuth tungstate surface in one of our previous study [47] and for methylene blue on niobium oxide ( $\text{Nb}_2\text{O}_5$ ) by another group [62]. Zhao et al. shows in this work that the degradation is not affected by the presence of DMSO which is known to be a radical scavenger and that consequently the mechanism is rather a direct transfer of photoinduced charge carriers on the pollutant. The same proposition can be done in the present system and the EPR experiments reported in the next section were performed to study the role of radicals in the degradation mechanism.

#### 3.4. Photogeneration of active radicals in water

Of course, the photocatalytic process may not be reduced to the study of the dye adsorption on the photocatalyst and the amount of photogenerated charge carriers at the surface of the semiconductor, is of particular importance to generate reactive radicals or to transfer directly on the pollutant. Indeed, the RhB oxidation occurs either directly with the photogenerated holes located on the titania surface or indirectly with other reactive species obtained from the surface activation of  $\text{H}_2\text{O}$  or  $\text{O}_2$ . As explained elsewhere [2,63] the hydroxyl radical  $\text{HO}^\bullet$  may be responsible for the indirect oxidation of organic species. That is why the amount of reactive oxygen species (ROS) created in solution is a key parameter and was measured by EPR [64]. A spin trapping molecule, the 5,5-dimethyl-1-pyrroline-*n*-oxide (DMPO) was used to stabilize the hydroxyl radical  $\text{HO}^\bullet$  through the formation of the spin adducts  $\cdot\text{DMPO}-\text{OH}$  that allows a quantification of the radical production in the studied titania samples under UV exposure (spectrum of the spin-adduct obtained with the P25 photocatalyst reported in the inset of Fig. 6). A quantitative comparison of the  $\cdot\text{DMPO}-\text{OH}$  production by all the samples for different UV irradiation exposure times is reported in Fig. 6.

The  $\cdot\text{DMPO}-\text{OH}$  adduct production cannot directly be correlated to the photocatalytic activity for RhB degradation. Indeed, for the same weight of  $\text{TiO}_2$ , the reference photocatalyst P25 produces twice more hydroxyl radicals than the AGlu sample for only half the photocatalytic efficiency in RhB degradation. The EPR measurements confirm that the RhB degradation occurs mainly through a direct charge carrier transfer at the particles surface, when the dye

is adsorbed on surfaces presenting the strongest surface acidity. However, the good photocatalytic efficiency of the AGlu sample cannot be generalized and another publication describing in details the photocatalytic efficiency of the AGlu sample on different photodegradation reactions show for instance that the phenol degradation is correlated to  $\text{HO}^\bullet$  production [66]. Indeed, the proposed degradation mechanism of this pollutant [67] require the presence of reactive radicals for an indirect degradation at low concentrations. Overall, all the characterizations presented are supporting that the most acidic sample AGlu exposing  $\{101\}$  faces is thus the best photocatalyst of our set of materials for a direct reduction of the RhB.

In order to explain the enhanced efficiency of the AGlu sample compared to ARods that also expose mainly the  $\{101\}$  faces, three parameters should be discussed: the specific area, the surface cleanliness and the different kind of steps observed on those  $\{101\}$  surfaces. The first parameter is in favor of AGlu with a specific surface 50% higher than ARods. Then, both samples were prepared in the presence of organic additives but FTIR show qualitatively cleaner surfaces for the AGlu sample. Finally the AGlu sample displays steps on  $\{101\}$  surfaces very similar to those observed on a very recent study [68]. They have experimentally and theoretically shown that those steps trap the photogenerated electrons and consequently the adsorption of  $\text{O}_2$  is favored. This point may also be crucial for the material efficiency for adsorbed oxygen may trap photogenerated electron thus avoiding charge recombination. The saw-like geometry of ARods surfaces with  $(101)$  and  $(10-1)$  alternate planes is relatively different and may trap less electron that are then more prone to recombine with holes.

The  $\text{AuW}$  sample should at least partly present the same acidic sites as the ARods sample for it also displays  $\{101\}$  surface but interestingly it does not exhibit any physisorption and Brønsted sites. The more interesting feature of this sample is that it presents two exposed crystallographic faces. With the FT-IR spectra, indeed, the two kinds of acidity noticed at  $1600$  and  $1040\text{ cm}^{-1}$  are specific to this sample and may be attributed to the  $\{100\}$  faces exposed by the rods population. The acidity corresponding to those bands and the lower photocatalytic efficiency when compared to AGlu may be explained by the sites of the  $\{100\}$  faces being less acidic than those of  $\{101\}$ . Indeed, previous DFT calculations on different anatase surfaces using the MUSIC showed that the  $\{100\}$  faces were relatively the most basic crystallographic faces [61].

The less efficient photocatalyst in the present study is the ACubes sample. Moreover, a slight blue-shift of the dye absorption peak was observed with this sample (cf absorption curves in Fig. S1-D). This shift can be associated to degradation pathway known as the N-deethylation process [69,70]. It corresponds to the absorption of a photon by the dye which is converted into an excited electron transferred to the titania conduction band, oxidizing the dye at the same time and thus leading to its degradation [37,47]. This mechanism may occur with a specific and strong adsorption of the dye and, in the present case, it is observed for the sample presenting the larger amount of adsorbed RhB (about 20% of the dye initially present). ACubes seem then to present a specific adsorption mode of the dye which is not observed for other samples. This adsorption seems to be efficient for the electron transfer from the dye to the semiconductor but less efficient to degrade the conjugated system of the dye. This morphology is the only one that presents significant amounts of the  $\{001\}$  faces. Several studies propose that surface as the most active one among the anatase facets which goes against the results of the present study [42,71–73]. However, the platelets exposing high amounts of  $\{001\}$  facets are synthesized using hydrofluoric acid as shaping agent and the cleaning steps generally give clean surface (yet, the  $\text{F}^-$  ions stabilizing the face may be accounted for a part of this activity) [9,10,42]. In the present case the protocol inspired from Sugimoto implies the presence of the

oleic acid molecules that favors the formation of the {0 0 1} faces but that may alter the photocatalytic efficiency of the sample. The issue is then that reactive faces such as {0 0 1} are difficult to obtain without reconstructions if a too harsh cleaning is used. It is then worth reminding here that a specific band in FT-IR was observed in that ACubes sample that could be responsible of another kind of acidic site. These sites may be responsible for the strong specific adsorption of the RhB via the amino group. A parallel can be drawn here with the efficiency of those different sets of particles in dye sensitized solar cells (DSSC) reported in a previous work [4]. The ACubes sample presented a better efficiency than the AGlu sample for it was able to adsorb higher amounts of the N719 dye and to ensure a better transfer of the harvested electrons. This clearly points out that the tuning of a material shape must be done specifically for a targeted application and in that case of photocatalysis for one targeted pollutant.

#### 4. Conclusions

The sol-gel synthesis techniques in aqueous medium were efficiently applied to obtain a set of four different morphologies of pure anatase nanoparticles. Three of the prepared samples were shown to efficiently degrade rhodamine B when compared to the P25 reference. A correlation between the nature of the exposed surfaces, the corresponding surface acidic behavior and the photocatalytic activity could be drawn. More precisely, the sample  $\text{A}_{\mu}\text{W}$  obtained by using the microwave oven exposing the less acidic {1 0 0} faces seems to be less efficient than AGlu exposing mainly the {1 0 1} ones. An additional coupling of those results with the quantification of ROS production by the different samples had us conclude that the tailoring of anatase exposed surface may be of paramount importance when considering the photodegradation of a pollutant that involve a direct transfer of photogenerated charge carriers on the adsorbed molecule. However, the conclusions of that study are specific to the pollutant targeted and the absolute efficiency of a defined photocatalyst should be determined with the use of different model pollutant and more specifically pollutant that do not absorb in the visible range and that weakly adsorb on the semi-conductors surfaces. This experimental study paves the way to a more theoretical approach of the selection of the best  $\text{TiO}_2$  photocatalyst morphology for a defined pollutant that may be degraded directly on the surface. Indeed, it may be interesting to study through first principle calculation the adsorption modes of a defined pollutant on the different surface of anatase in order to predict the place where the charge carrier transfer is the more efficient. The experimental methodology, on the well-known anatase structure could also be transferred on other photocatalysts to enhance their efficiencies without using dopants or making heterostructures.

#### Associated content

Detailed information concerning the UV-vis spectrum of the lamp used for photocatalysis, the Raman spectra of the  $\text{TiO}_2$  samples, maximum anisotropic ratio of anatase bipyramids, snapshots of TEM tomography of the ACube sample, TEM image of ACubes sample with smoother washing, UV-vis photodegradation spectra with the different samples and experimental conditions, FT-IR spectra of the samples after activation in the measurement cell,  $\nu_{19b}$  and  $\nu_{8a}$  pyridine vibration mode.

#### Acknowledgments

We are very grateful to the European Multifunctional Materials Institute (EMMI) for encouraging and financially supporting this

work through the Erasmus Mundus International Doctoral School IDS-FunMat and to the University Pierre et Marie Curie (UPMC), Paris. The authors also greatly acknowledge the financial support of this work by the French ANR within the Photonorm project (ANR-11-ECOT-0008) and the Mesonnet project (ANR-10-NANO-0006).

#### Appendix A. Supplementary data

Supplementary data associated with this article can be found, in the online version, at <http://dx.doi.org/10.1016/j.apcatb.2015.03.013>.

#### References

- [1] X. Chen, S.S. Mao, Chem. Rev. 107 (2007) 2891–2959.
- [2] A. Fujishima, X. Zhang, D.A. Tryk, Surf. Sci. Rep. 63 (2008) 515–582.
- [3] S. Ito, T.N. Murakami, P. Comte, P. Liska, C. Grätzel, M.K. Nazeeruddin, M. Grätzel, Thin Solid Films 516 (2008) 4613–4619.
- [4] C. Magne, F. Dufour, F. Labat, G. Lancel, O. Durupthy, S. Cassaignon, T. Pauporté, J. Photochem. Photobiol. A 232 (2012) 22–31.
- [5] M. Koelsch, S. Cassaignon, C.T.T. Minh, J.F. Guillemoles, J.P. Jolivet, Thin Solid Films 452 (2004) 86–92.
- [6] O.O. Prieto-Mahaney, N. Murakami, R. Abe, B. Ohtani, Chem. Lett. 38 (2009) 7–8.
- [7] Q. Sun, Y. Xu, J. Phys. Chem. C 114 (2010) 18911–18918.
- [8] H. Zhang, J. Banfield, J. Mater. Chem. 8 (1998) 2073–2076.
- [9] Y. Luan, L. Jing, Y. Xie, X. Sun, Y. Feng, H. Fu, ACS Catal. 3 (6) (2013) 1378.
- [10] J. Pan, G. Liu, G. Qing, M. Lu, H.-M. Cheng, Angew. Chem. Int. Ed. 50 (2011) 2133–2137.
- [11] C. Colbeau-Justin, M. Kunst, D. Huguenin, J. Mater. Sci. 11 (2003) 2429–2437.
- [12] J.P. Jolivet, Metal Oxide Chemistry and Synthesis. From Solution to Solid State, Wiley, Chichester, 2000.
- [13] T. Sugimoto, X. Zhou, A. Muramatsu, J. Colloid Interface Sci. 252 (2002) 339–346.
- [14] F. Dufour, S. Cassaignon, O. Durupthy, C. Colbeau-Justin, C. Chanéac, Eur. J. Inorg. Chem. 2012 (16) (2012) 2707–2715.
- [15] O. Durupthy, J. Bill, F. Aldinger, Cryst. Growth Des. 7 (2007) 2696–2704.
- [16] T. Sugimoto, J. Colloid Interface Sci. 259 (2003) 53–61.
- [17] A. Pottier, C. Chanéac, E. Tronc, L. Mazerolles, J.-P. Jolivet, J. Mater. Chem. 11 (2001) 1116–1121.
- [18] M. Lazzeri, A. Vittadini, A. Selloni, Phys. Rev. B 63 (2001) 155409.
- [19] U. Diebold, Surf. Sci. Rep. 48 (2003) 53–229.
- [20] P.D. Cozzoli, A. Kornowski, H. Weller, J. Am. Chem. Soc. 125 (2003) 14539–14548.
- [21] Y.-W. Jun, M.F. Casula, J.-H. Sim, S.Y. Kim, J. Cheon, A.P. Alivisatos, J. Am. Chem. Soc. 125 (2003) 15981–15985.
- [22] K. Kanie, T. Sugimoto, Chem. Commun. 2004 (14) (2004) 1584–1585.
- [23] X.-L. Li, Q. Peng, J.-X. Yi, X. Wang, Y. Li, Chem. Eur. J. 12 (2006) 2383–2391.
- [24] R. Buonsanti, E. Carlino, C. Giannini, D. Altamura, L. De Marco, R. Giannuzzi, M. Manca, G. Gigli, P.D. Cozzoli, J. Am. Chem. Soc. 133 (2011) 19216–19239.
- [25] Y. Liang, S. Gan, S.A. Chambers, E.I. Altman, Phys. Rev. B 63 (2001) 235402.
- [26] C. Deiana, E. Fois, S. Coluccia, G. Martra, J. Phys. Chem. C 114 (2010) 21531–21538.
- [27] D.C. Hurum, A.G. Agrios, K.A. Gray, T. Rajh, M.C. Thurnauer, J. Phys. Chem. B 107 (2003) 4545–4549.
- [28] D.C. Hurum, K.A. Gray, T. Rajh, M.C. Thurnauer, J. Phys. Chem. B 109 (2005) 977–980.
- [29] B. Ohtani, D. Li, R. Abe, J. Photochem. Photobiol. A 216 (2010) 179–182.
- [30] S.T. Martin, H. Herrmann, W.Y. Choi, M.R. Hoffmann, J. Chem. Soc. Faraday Trans. 90 (1994) 3315–3322.
- [31] S.T. Martin, H. Herrmann, M.R. Hoffmann, J. Chem. Soc. Faraday Trans. 90 (1994) 3323–3330.
- [32] Z. Zhang, C.-C. Wang, R. Zakaria, J.Y. Ying, J. Phys. Chem. B 102 (1998) 10871–10878.
- [33] N. Satoh, T. Nakashima, K. Kamikura, K. Yamamoto, Nat. Nanotechnol. 3 (2008) 106–111.
- [34] C. Colbeau-Justin, M. Kunst, D. Huguenin, J. Mater. Sci. 38 (2003) 2429–2437.
- [35] A.V. Vorontsov, A.A. Altynnikov, E.N. Savinov, E.N. Kurkin, J. Photochem. Photobiol. A 144 (2001) 193–196.
- [36] F. Chen, J. Zhao, H. Hidaka, Int. J. Photoenergy 5 (2003) 209–217.
- [37] S. Pigeot-Rémy, F. Dufour, A. Herrissan, S. Kathoum, V. Ruaux, F. Maugé, O. Durupthy, C. Colbeau-Justin, C. Guillard, C. Forronato, R. Hazime, S. Cassaignon, C. Chaneac, J. Catal. (2015), submitted.
- [38] C. Minero, F. Catocco, E. Pelizzetti, C. Analitica, U. Torino, Langmuir 8 (2) (1992) 481–486.
- [39] J.-M. Herrmann, J. Photochem. Photobiol. A 216 (2010) 85–93.
- [40] S. Pigeot-Rémy, F. Dufour, A. Herrissan, S. Kathoum, V. Ruaux, F. Maugé, O. Durupthy, C. Colbeau-Justin, C. Guillard, C. Forronato, R. Hazime, S. Cassaignon, C. Chaneac, J. Catal. (2014), submitted.
- [41] S. Pigeot-Rémy, F. Dufour, A. Herrissan, S. Kathoum, V. Ruaux, F. Maugé, O. Durupthy, C. Colbeau-Justin, C. Guillard, C. Forronato, R. Hazime, S. Cassaignon, C. Chaneac, J. Catal. (2014), submitted.
- [42] S. Liu, J. Yu, M. Jaroniec, Chem. Mater. 23 (2011) 4085–4093.

- [43] T. Hiemstra, P. Venema, W.H.V. Riemsdijk, *J. Colloid Interface Sci.* 184 (1996) 680–692.
- [44] T. Hiemstra, W.H. Van Riemsdijk, G.H. Bolt, *J. Colloid Interface Sci.* 133 (1989) 91–104.
- [45] D. Chiche, C. Chizallet, O. Durupthy, C. Chanéac, R. Revel, P. Raybaud, J.-P. Jolivet, *Phys. Chem. Chem. Phys.* 11 (2009) 11310–11323.
- [46] J.-P. Jolivet, C. Froidefond, A. Pottier, C. Chanéac, S. Cassaignon, E. Tronc, P. Euzen, *J. Mater. Chem.* 14 (2004) 3281–3288.
- [47] T. Saison, N. Chemin, C. Chan, O. Durupthy, L. Mariey, *J. Phys. Chem. C* 115 (2011) 5657–5666.
- [48] J.-P. Jolivet, C. Chaneac, D. Chiche, S. Cassaignon, O. Durupthy, J. Hernandez, C. R. Geosci. 343 (2011) 113–122.
- [49] G. Busca, *Phys. Chem. Chem. Phys.* 1 (1999) 723–736.
- [50] A.M. Turek, I. Wachs, E. DeCanio, *J. Phys. Chem.* 96 (1992) 5000–5007.
- [51] A. Vimont, J.-C. Lavalle, D. Dambourret, M. Nickkho-amiry, J.M. Winfield, *Phys. Chem. Chem. Phys.* 11 (2009) 1369–1379.
- [52] M.I. Zaki, M.A. Hasan, F.A. Al-sagheer, L. Pasupulety, *Colloids Surf. A* 190 (2001) 261–274.
- [53] C. Morterra, *J. Chem. Soc. Faraday Trans. 1* (84) (1988) 1617–1637.
- [54] E.P. Parry, *J. Catal.* 2 (1963) 371–379.
- [55] S. Dzwigaj, C. Arrouvel, M. Breysse, C. Geantet, S. Inoue, H. Toulhoat, P. Raybaud, *J. Catal.* 236 (2005) 245–250.
- [56] C. Chizallet, G. Costentin, M. Che, F. Delbecq, P. Sautet, *J. Am. Chem. Soc.* 129 (2007) 6442–6452.
- [57] A. Travert, A. Vimont, A. Sahibed-dine, M. Daturi, J.-C. Lavalle, *Appl. Catal. A* 307 (2006) 98–107.
- [58] T. Saison, P. Gras, N. Chemin, C. Chanéac, O. Durupthy, V. Brezova, C. Colbeau-Justin, J.-P. Jolivet, *J. Phys. Chem. C* 117 (2013) 22656–22666.
- [59] P.O. Scokart, P.G. Rouxhet, *J. Colloid Interface Sci.* 86 (1982) 96.
- [60] H. Leclerc, A. Vimont, J.-C. Lavalle, M. Daturi, A.D. Wiersum, P.L. Llewellyn, P. Horcajada, G. Férey, C. Serre, *Phys. Chem. Chem. Phys.* 13 (2011) 11748–11756.
- [61] M.A. Ahmad, B. Prelot, F. Dufour, O. Durupthy, A. Razafitianamaharavo, J.M. Douillard, C. Chaneac, F. Villiéras, J. Zajac, *J. Phys. Chem. C* 117 (2013) 4459–4469.
- [62] Y. Zhao, C. Eley, J. Hu, J.S. Foord, L. Ye, H. He, S.C.E. Tsang, *Angew. Chem. Int. Ed.* 51 (2012) 3846–3849.
- [63] M.A. Henderson, *Surf. Sci. Rep.* 66 (2011) 185–297.
- [64] J.-M. Herrmann, *Top. Catal.* 34 (2005) 49–65.
- [65] D. Dvoranová, V. Brezová, M. Mazúr, M.A. Malati, *Appl. Catal. B* 37 (2002) 91–105.
- [66] S. Piguet-Rémy, F. Dufour, A. Herrissan, S. Kathoum, V. Ruaux, F. Maugé, O. Durupthy, C. Colbeau-Justin, C. Guillard, C. Forronato, R. Hazime, S. Cassaignon, C. Chaneac, *J. Catal.* (2013), submitted.
- [67] J. Moreira, B. Serrano, A. Ortiz, H. de Lasa, *Chem. Eng. Sci.* 78 (2012) 186–203.
- [68] M. Setvin, X.F. Hao, B. Daniel, J. Pavelec, Z. Novotny, G.S. Parkinson, M. Schmid, G. Kresse, C. Franchini, U. Diebold, *Angew. Chem. Int. Ed.* 53 (2014) 4714–4716.
- [69] T. Wu, G. Liu, J. Zhao, H. Hidaka, N. Serpone, *J. Phys. Chem. B* 102 (1998) 5845–5851.
- [70] P. Qu, J.C. Zhao, T. Shen, H. Hidaka, *J. Mol. Catal. A: Chem.* 129 (1998) 257–268.
- [71] Y. Dai, C.M. Cobley, J. Zeng, Y. Sun, Y. Xia, *Nano Lett.* 9 (2009) 2455–2459.
- [72] J. Li, D. Xu, *Chem. Commun.* 46 (2010) 2301–2303.
- [73] Z. Zhao, Z. Sun, H. Zhao, M. Zheng, P. Du, J. Zhao, H. Fan, *J. Mater. Chem.* 22 (2012) 21965–21971.